Phase-dependent growth of Pt on MoS_2 for highly efficient H_2 evolution

Zhenyu Shi[1,2†], Xiao Zhang[3†], Xiaoqian Lin[4†], Guigao Liu[1†], Chongyi Ling[1,5†], Shibo Xi[6†], Bo Chen[1], Yiyao Ge[1], Chaoliang Tan[1], Zhuangchai Lai[1], Zhiqi Huang[1], Xinyang Ruan [1], Li Zhai[1,7], Lujiang Li[1], Zijian Li[1], Xixi Wang[1], Gwang-Hyeon Nam[2], Jiawei Liu[2], Qiyuan He[8], Zhiqiang Guan[1,9], Jinlan Wang[5], Chun-Sing Lee[1,9], Anthony R. J. Kucernak[4]* and Hua Zhang[1,7,10]*

[1]Department of Chemistry, City University of Hong Kong, Hong Kong, China.

[2]Center for Programmable Materials, School of Materials Science and Engineering, Nanyang Technological University, Singapore 639798, Singapore.

[3]Department of Mechanical Engineering, The Hong Kong Polytechnic University, Hung Hom, Kowloon, Hong Kong, China.

[4]Department of Chemistry, Molecular Science Research Hub, Imperial College London, W12 0BZ, U.K.

[5]School of Physics, Southeast University, Nanjing 211189, China.

[6]Institute of Chemical and Engineering Science, A*STAR (Agency for Science, Technology and Research), Singapore 627833, Singapore.

[7]Hong Kong Branch of National Precious Metals Material Engineering Research Center (NPMM), City University of Hong Kong, Hong Kong, China.

[8]Department of Materials Science and Engineering, City University of Hong Kong, Hong Kong, China.

[9]Center of Super-Diamond and Advanced Films (COSDAF), City University of Hong Kong, Hong Kong, China.

[10]Shenzhen Research Institute, City University of Hong Kong, Shenzhen, 518057, China.

*Correspondence author. Email: hua.zhang@cityu.edu.hk, anthony@imperial.ac.uk

[†]These authors contributed equally to this work.

Crystal phase is a key factor determining the properties and hence function of two-dimensional (2D) transition-metal dichalcogenides (TMDs)[1,2]. The materials, explored for diverse applications[3,4,6-9], commonly serve as templates for constructing nanomaterials[3-5] and supported metal catalysts[4,7-9]. But how the TMD crystal phase affects the growth of the secondary material is poorly understood, though relevant particularly for catalyst development. In the case of Pt nanoparticles on 2D MoS_2 nanosheets used as electrocatalysts for the hydrogen evolution reaction (HER)[8], only about 2/3 of Pt nanoparticles were epitaxially grown on the MoS_2 template comprised of the metallic/semimetallic 1T/1T′ phase but with thermodynamically stable and poorly conducting 2H phase mixed in[10,11]. Here, we report the production of MoS_2 nanosheets with high phase purity and show that the 2H phase templates epitaxial growth of Pt nanoparticles whereas the 1T′ phase supports single-atomically dispersed Pt atoms with loadings up to 10 wt%. We find that the Pt atoms in this s-Pt/1T′-MoS_2 system occupy three distinct sites, with DFT calculations indicating for Pt atoms located atop of Mo atoms a hydrogen adsorption free energy of close to zero. This likely contributes to efficient H_2 evolution in acidic media, where we measure for s-Pt/1T′-MoS_2 a mass activity of 85±23 A mg_{Pt}^{-1} at the overpotential of -50 mV, a mass-normalized exchange current density of 127 A mg_{Pt}^{-1} and see stable performance in an H-type cell and prototype proton exchange membrane electrolyser operated at room temperature. Although phase stability limitations prevent operation at high temperatures, we anticipate that 1T′-TMDs will be effective supports also for other catalysts targeting other important reactions.

The preparation of 1T′-MoS_2 nanosheets (NSs) is illustrated in Fig. 1a (see Materials synthesis in Methods for details). Briefly, the tetraheptylammonium bromide molecules were first intercalated into K_xMoS_2 crystals (Supplementary Fig. 1) in an electrochemical cell (Step 1 in Fig. 1a). After the exfoliation (Step 2 in Fig. 1a), 1T′-MoS_2 NSs (Fig. 1b) with a thickness of 1.4±0.4 nm (Fig. 1c,d) and lateral size of up to several micrometers (Supplementary Fig. 2)

were prepared. The aberration-corrected high-angle annular dark-field scanning transmission electron microscopy (HAADF-STEM) image (Fig. 1e and Supplementary Fig. 3a) shows the zigzag chains with the shortest Mo-Mo distance of 2.78 Å (Supplementary Fig. 3b), which is consistent with the theoretical 1T′-MoS_2 structure (Supplementary Fig. 4a). The corresponding fast Fourier transform (FFT) pattern (inset of Fig. 1e) and the selected area electron diffraction (SAED) pattern (Supplementary Fig. 5) further confirm the distorted octahedral coordinated structure and the high crystallinity of the obtained 1T′-MoS_2 NSs. The uniform elemental distribution of Mo and S elements with a Mo/S ratio of ~1:2 is confirmed by the energy-dispersive X-ray spectroscopy (EDS) (Supplementary Fig. 6). The EDS (Supplementary Fig. 6d) and X-ray photoelectron spectroscopy (XPS) (Supplementary Fig. 7) results show no detectable potassium, bromide and other residues in the obtained 1T′-MoS_2 NSs, indicating the high purity of 1T′-MoS_2 NSs. By using the same method (see Materials synthesis in Methods for details), highly crystalline 2H-MoS_2 NSs with a thickness of 1.9±0.4 nm have also been prepared from the commercial 2H-MoS_2 powder (Extended Data Fig. 1).

The phase purity of the 1T′-MoS_2 and 2H-MoS_2 NSs was further characterized. The ultraviolet-visible (UV-Vis) absorption spectrum (Supplementary Fig. 8) gives the featureless absorption of 1T′-MoS_2 NS dispersion, indicating its metallic nature, while the 2H-MoS_2 NS dispersion shows four featured peaks located at 400, 454, 618, and 675 nm, respectively[12,13]. The XPS spectra of 1T′-MoS_2 NSs (Fig. 1f) show that both binding energies of Mo $3d_{5/2}$ and Mo $3d_{3/2}$, *i.e.*, 228.7 eV, and 231.8 eV, respectively, shift to lower values by ~0.8 eV as compared to that of 2H-MoS_2, which is consistent with a previous report[10]. In addition, the Raman spectrum of 1T′-MoS_2 NSs exhibits five characteristic peaks, *i.e.*, 151.8 (J_1), 213.6 (J_2), 280.8, 328.4 (J_3), and 404.1 (A_{1g}) cm^{-1}, respectively (Fig. 1g), matching well with the previous reports[10,11,14]. Importantly, the characteristic E^1_{2g} peak of 2H-MoS_2 (382.8 cm^{-1}) is absent, confirming the high phase purity of the 1T′-MoS_2 NSs. Differently, two characteristic Raman peaks, *i.e.*, 382.8 cm^{-1} (E^1_{2g}) and 407.8 cm^{-1} (A_{1g}), are clearly observed in the 2H-MoS_2 NSs (Fig. 1g). These results confirm that the 1T′-MoS_2 and 2H-MoS_2 NSs with high phase purity and high

crystallinity have been prepared.

Pt with similar loading was then deposited on these ideal templates via photoreduction (see Materials synthesis in Methods for details). When using 2H-MoS_2 NSs, ultra-small PtNPs with an average size of 1.1±0.4 nm (Extended Data Fig. 2 and Supplementary Fig. 9) grew epitaxially on the template with a Pt loading amount of ~9.6 wt%, with the hybrid material denoted as PtNPs/2H-MoS_2 (Supplementary Table 1). In contrast, with 1T′-MoS_2 NSs as templates, Pt with a loading of ~10.0 wt% was single-atomically dispersed on the template and is denoted as s-Pt/1T′-MoS_2 (Supplementary Table 1). No PtNPs can be observed on the surface of 1T′-MoS_2 (Fig. 2a), and no diffraction spots assigned to PtNPs can be found in the SAED pattern (inset of Fig. 2a). The EDS mapping images (Fig. 2b) confirm the presence and homogeneous dispersion of Pt on the 1T′-MoS_2 NSs. Pt atoms exhibit much stronger brightness than Mo atoms and can be easily distinguished in the aberration-corrected HAADF-STEM characterization (Supplementary Fig. 10), revealing that Pt atoms were single-atomically dispersed on 1T′-MoS_2 occupies three different locations (Fig. 2c): Pt substituting Mo site (Pt_{sub}), Pt adsorbed on the top site of S ($Pt_{ads\text{-}S}$), and Pt adsorbed on the top site of Mo ($Pt_{ads\text{-}Mo}$). The optimized density functional theory (DFT) models (Fig. 2d_1-f_1 and Supplementary Fig. 11) illustrate the details of the bonding environment of Pt_{sub}, $Pt_{ads\text{-}S}$, and $Pt_{ads\text{-}Mo}$. The simulated intensity profiles (dashed curves in Fig. 2d_3-f_3) taken from the simulated STEM images (Fig. 2d_2-f_2) based on the DFT models (Fig. 2d_1-f_1) show good agreement with the experimental intensity profiles (histograms in Fig. 2d_3-f_3) which are taken from the corresponding white dotted rectangles in Fig. 2c.

The X-ray absorption near-edge spectroscopy (XANES) and extended X-ray absorption fine structure (EXAFS) profiles were used to investigate the electronic structure and coordination of the Pt in s-Pt/1T′-MoS_2 and PtNPs/2H-MoS_2. As shown in Fig. 3a, the height of the white line of Pt L_3-edge XANES of s-Pt/1T′-MoS_2 is closer to that of PtS_2 and significantly higher than that of Pt foil, indicating the Pt species in the s-Pt/1T′-MoS_2 are dominantly in the oxidized state. The Fourier-transformed EXAFS of s-Pt/1T′-MoS_2 exhibits a dominant peak at 1.87 Å (Fig. 3b), which can be attributed to the Pt-S contribution[15]. The fitting results (Supplementary

Fig. 12 and Supplementary Table 2) demonstrate that the Pt-S bond has an average bond length of 2.30 Å and an average coordination number of 4.2 in the s-Pt/1T′-MoS_2. There is no peak attributable to the metallic Pt-Pt bond, further confirming the single-atomically dispersed Pt on 1T′-MoS_2 NSs[7,16]. In addition, the good agreement between the experimental and simulated XANES curves (Supplementary Fig. 13) affirms three kinds of Pt atoms (Pt_{sub}, $Pt_{ads\text{-}S}$, and $Pt_{ads\text{-}Mo}$) coexisting in the s-Pt/1T′-MoS_2, which is consistent with the HAADF-STEM analysis (Fig. 2). However, as for the PtNPs/2H-MoS_2, the Pt L_3-edge XANES is identical with that of Pt foil (Fig. 3a), suggesting that the Pt species are mainly in the metallic state. Moreover, a dominant peak at 2.45 Å is observed in the Fourier-transformed EXAFS of PtNPs/2H-MoS_2 (Fig. 3b), further revealing the formation of Pt-Pt metallic bond in the PtNPs (Supplementary Fig. 12 and Supplementary Table 2).

XPS was further used to reveal the valence states of Pt and Mo in the synthesized Pt-MoS_2 hybrids. As shown in Fig. 3c, the fitted peaks of Pt $4f_{7/2}$ located at 72.5 eV, 73.5 eV, and 74.8 eV can be assigned to $Pt^{\delta+}$, Pt^{2+}, and Pt^{4+}, respectively[17,18], suggesting the formation of Pt-S bond. On the contrary, a strong fitted Pt^0 peak of Pt $4f_{7/2}$ located at 71.8 eV is observed in the XPS spectrum of PtNPs/2H-MoS_2 besides the weak $Pt^{\delta+}$, Pt^{2+}, and Pt^{4+} peaks, indicating the dominant metallic state of PtNPs grown on 2H-MoS_2. In addition, the Mo 3*d* XPS (Fig. 3d) and Raman spectra (Supplementary Fig. 14) confirm that no phase transition occurred in the 1T′-MoS_2 and 2H-MoS_2 NSs after they were used as templates to grow Pt.

s-Pt can be deposited on 1T′-MoS_2 NSs with lower Pt loadings of 4.3 wt% (denoted as s-Pt-4/1T′-MoS_2, Extended Data Fig. 3) and 6.4 wt% (denoted as s-Pt-6/1T′-MoS_2, Extended Data Fig. 4). But when increasing the Pt loading above 10.0 wt%, PtNPs form as seen for 1T′-MoS_2 NSs with Pt loadings of 12.2 wt% (denoted as PtNPs-12/1T′-MoS_2, Extended Data Fig. 5) and 15.5 wt% (denoted as PtNPs-15/1T′-MoS_2, Extended Data Fig. 6). The EDS mapping results (Extended Data Figs. 3b-6b) show the distribution of Pt elements on the 1T′-MoS_2 NSs. Furthermore, the Raman spectra (Extended Data Figs. 3c-6c) and Mo 3*d* XPS spectra (Extended Data Figs. 3d-6d) confirm that no phase transition occurred in the 1T′-MoS_2 NSs

after they were used as templates to grow Pt. In the Pt 4*f* XPS spectra (Extended Data Fig. 7), only Pt with oxidation states can be observed for s-Pt-4/1T′-MoS_2 and s-Pt-6/1T′-MoS_2. In contrast, strong Pt^0 peaks can be observed in PtNPs-12/1T′-MoS_2 and PtNPs-15/1T′-MoS_2. These observations illustrate that the amount of Pt loaded onto 1T′-MoS_2 NSs and the Pt structure can be controlled.

Due to their outstanding HER performance, activities of Pt-based electrocatalysts measured in acidic media tend to be affected by mass transport limitation[19,20]. To minimize this limitation, we used the floating electrode technique[21] to evaluate the performance of s-Pt/1T′-MoS_2 as HER electrocatalyst in acidic media, with commercial HiSPEC 9100 Pt/C as a reference. The scheme and photograph of a typical floating electrode setup are shown in Fig. 4a and Supplementary Fig. 15, respectively (see Electrochemical measurements in Methods for details). Three batches of floating electrodes were prepared for s-Pt/1T′-MoS_2 and HiSPEC 9100 Pt/C (Electrodes 1-6, denoted as **E1**-**E6**, respectively, Supplementary Table 3), with ultra-low Pt loadings ensuring that the HER measurements at -50 mV were under the kinetic control and not limited by mass transport. Fig. 4b,c show the HER polarization curves of s-Pt/1T′-MoS_2 on **E1** (Pt loading of 398 $ng_{Pt}\ cm^{-2}$) and HiSPEC 9100 Pt/C on **E2** (Pt loading of 286 $ng_{Pt}\ cm^{-2}$), with results for electrodes **E3-E6** shown in Supplementary Figs. 16 and 17. As seen in Fig. 4b, the geometric current density ($j_{geometric}$) of s-Pt/1T′-MoS_2 increases exponentially with overpotential. Even at a high current density (500 mA cm^{-2}), the cyclic voltammogram (CV) of s-Pt/1T′-MoS_2 (inset of Fig. 4b) shows almost no hysteresis between the anodic and cathodic scans. These results indicate that the HER measurements are not limited by bulk mass transport[19]. When comparing performance, s-Pt/1T′-MoS_2 and HiSPEC 9100 Pt/C require an overpotential of -19±5 mV and -24±3 mV to reach $j_{geometric}$ of 10 mA cm^{-2}, respectively. In terms of mass activity, s-Pt/1T′-MoS_2 reaches 85±23 A mg_{Pt}^{-1} at an overpotential of -50 mV for a floating electrode loading range of 533±118 $ng_{Pt}\ cm^{-2}$; in comparison, HiSPEC 9100 Pt/C with a floating electrode loading range of 563±273 $ng_{Pt}\ cm^{-2}$ reaches only 70±17 A mg_{Pt}^{-1} (Fig. 4c, Supplementary Figs. 16, 17). A comparison of mass activities of s-Pt/1T′-MoS_2 and HiSPEC 9100 Pt/C with those of previously reported Pt-based electrocatalysts for HER in

acidic media is provided in Fig. 4d (Ref [9,19,22-26]) and Supplementary Table 4.

To further evaluate the activity of s-Pt/1T′-MoS_2, a recently developed model[27] was used to calculate the mass-normalized exchange current density ($j_{0,mass}$) and Tafel slope from the mass activities. As shown in Fig. 4e,f, the fitted curves show good agreement with experimental data. The calculated Tafel slope of s-Pt/1T′-MoS_2 is 118 mV dec^{-1}, which matches well with that tested using H_2 pump technique[28]. Moreover, the s-Pt/1T′-MoS_2 exhibits a $j_{0,mass}$ of 127 A mg_{Pt}^{-1}, which is 2-3 orders of magnitude higher than those obtained from the conventional static electrode and rotating disk electrode technique[21,29-32] and in the same order of magnitude as those obtained from other high mass transport techniques (Fig. 4g and Supplementary Table 5)[21,28,33,34].

Furthermore, the stability of s-Pt/1T′-MoS_2 during HER was evaluated. As shown in Supplementary Fig. 18, the polarization curve exhibits no obvious degradation after 10,000 cyclic voltammetry cycles. The XANES (Extended Data Fig. 8a), EXAFS (Extended Data Fig. 8b,c), XPS (Supplementary Figs. 19 and 20) and Raman results (Supplementary Fig. 21) indicate that Pt in s-Pt/1T′-MoS_2 remains single-atomically dispersed and 1T′-MoS_2 preserves its structure after the durability test. Transmission electron microscopy (TEM), high-resolution TEM (HRTEM) and EDS mapping results (Supplementary Fig. 22) show that no PtNP is found in s-Pt/1T′-MoS_2 after the durability test, with HAADF-STEM and statistical analysis (Extended Data Fig. 9) confirming that Pt_{sub}, $Pt_{ads\text{-}S}$ and $Pt_{ads\text{-}Mo}$ are still present.

To further understand the HER activity of s-Pt/1T′-MoS_2, DFT calculations were conducted based on the established DFT models of isolated $Pt_{ads\text{-}S}$ (Fig. 2e$_1$ and Extended Data Fig. 10a), isolated $Pt_{ads\text{-}Mo}$ (Fig. 2f$_1$ and Extended Data Fig. 10b), and Pt_{sub}+$Pt_{ads\text{-}S}$+$Pt_{ads\text{-}Mo}$ (Supplementary Fig. 13b). In order to distinguish from the isolated $Pt_{ads\text{-}S}$ and $Pt_{ads\text{-}Mo}$, the $Pt_{ads\text{-}S}$ and $Pt_{ads\text{-}Mo}$ in the Pt_{sub}+$Pt_{ads\text{-}S}$+$Pt_{ads\text{-}Mo}$ are denoted as $Pt'_{ads\text{-}S}$ and $Pt'_{ads\text{-}Mo}$, respectively (Extended Data Fig. 10c). First, the free energy for hydrogen adsorption (ΔG_H)[29,35], was calculated to evaluate the HER activity. The calculated ΔG_H diagram of $Pt_{ads\text{-}S}$, $Pt_{ads\text{-}Mo}$, $Pt'_{ads\text{-}S}$, and $Pt'_{ads\text{-}Mo}$ sites compared to Pt (111) is shown in Extended Data Fig. 10d. The ΔG_H of $Pt_{ads\text{-}}$

191 $_{Mo}$ (-0.07 eV) and $Pt'_{ads\text{-}Mo}$ (0.04 eV) are closer to 0 eV as compared to the Pt(111) (-0.11 eV),
192 which could enable faster hydrogen adsorption and product release on the $Pt_{ads\text{-}Mo}$ and $Pt'_{ads\text{-}Mo}$
193 sites. Furthermore, the *d*-band center (ε_d) was calculated to explain the variation of ΔG_H of the
194 s-Pt in s-Pt/1T′-MoS_2 (Extended Data Fig. 10e). Compared to the Pt(111), the shift of ε_d of
195 $Pt_{ads\text{-}S}$, $Pt_{ads\text{-}Mo}$, $Pt'_{ads\text{-}S}$ and $Pt'_{ads\text{-}Mo}$ to lower energies indicates the weaker hydrogen binding
196 strength of the s-Pt in s-Pt/1T′-MoS_2. With the downshift of ε_d, the ΔG_H of the $Pt_{ads\text{-}Mo}$ and
197 $Pt'_{ads\text{-}Mo}$ close to thermoneutral could contribute to the HER activity of the s-Pt/1T′-MoS_2.

198 More importantly, the HER activity and stability of the s-Pt/1T′-MoS_2 catalyst at high current
199 densities were also investigated in an H-type cell (see Electrochemical measurements in
200 Methods for details). The polarization curves (Supplementary Fig. 23a) indicate that the s-
201 Pt/1T′-MoS_2 can reach high current densities of 1,000, 1,500, and 2,000 mA cm^{-2} at low
202 overpotentials of about -91, -112 and -131 mV, respectively, which are lower than those
203 obtained on the commercial HiSPEC 9100 Pt/C catalyst. A detailed comparison of high-
204 current-density HER performances of our work with previous reports is given in
205 Supplementary Table 6. Furthermore, the chronopotentiometric test reveals the long-term
206 stability of s-Pt/1T′-MoS_2 at a current density of 1,500 mA cm^{-2}. After 240-h test, the
207 polarization curve exhibits a negligible shift (Supplementary Fig. 23b) and the overpotential
208 shows no obvious degradation (Supplementary Fig. 23c). As shown in the Supplementary
209 Video, H_2 bubbles are continuously produced and released from the surface of s-Pt/1T′-MoS_2
210 electrode during the electrocatalytic hydrogen evolution at 1,500 mA cm^{-2} in an H-type cell.

211 To explore the potential application of the s-Pt/1T′-MoS_2 catalyst, we fabricated a prototype
212 proton exchange membrane (PEM) electrolyser with s-Pt/1T′-MoS_2 as the cathode catalyst
213 (Supplementary Fig. 24, see Electrochemical measurements in Methods for details). Although
214 PEM water electrolysers typically operate at temperatures of 50 to 80 °C, preparation and
215 measurement of s-Pt/1T′-MoS_2 catalysts were conducted at room temperature to maintain the
216 1T′ phase that was shown[10] to start transitioning to the 2H phase at ~60 °C). Supplementary
217 Figs. 25a,b show that the cell voltages required to reach 500 mA cm^{-2} and 1,000 mA cm^{-2} are
218 only 1.73 V and 1.82 V (iR-corrected), respectively, while Supplementary Fig. 25c documents

219 that s-Pt/1T′-MoS_2 performs steadily for 500 h when operated at 100 mA cm^{-2} (with a detailed
220 comparison against the performance of previously reported 2D electrocatalysts given in
221 Supplementary Table 7).
222

References

1 Chhowalla, M. *et al.* The chemistry of two-dimensional layered transition metal dichalcogenide nanosheets. *Nat. Chem.* **5**, 263-275 (2013).

2 Chen, Y. *et al.* Phase engineering of nanomaterials. *Nat. Rev. Chem.* **4**, 243-256 (2020).

3 Novoselov, K. S., Mishchenko, A., Carvalho, A. & Castro Neto, A. H. 2D materials and van der Waals heterostructures. *Science* **353**, aac9439 (2016).

4 Liu, G. *et al.* MoS_2 monolayer catalyst doped with isolated Co atoms for the hydrodeoxygenation reaction. *Nat. Chem.* **9**, 810-816 (2017).

5 Sun, Y. *et al.* Interface-mediated noble metal deposition on transition metal dichalcogenide nanostructures. *Nat. Chem.* **12**, 284-293 (2020).

6 Geim, A. K. & Grigorieva, I. V. Van der Waals heterostructures. *Nature* **499**, 419-425 (2013).

7 Li, H. *et al.* Synergetic interaction between neighbouring platinum monomers in CO_2 hydrogenation. *Nat. Nanotechnol.* **13**, 411-417 (2018).

8 Huang, X. *et al.* Solution-phase epitaxial growth of noble metal nanostructures on dispersible single-layer molybdenum disulfide nanosheets. *Nat. Commun.* **4**, 1444 (2013).

9 Shi, Y. *et al.* Site-specific electrodeposition enables self-terminating growth of atomically dispersed metal catalysts. *Nat. Commun.* **11**, 4558 (2020).

10 Yu, Y. *et al.* High phase-purity 1T′-MoS_2- and 1T′-$MoSe_2$-layered crystals. *Nat. Chem.* **10**, 638-643 (2018).

11 Liu, L. *et al.* Phase-selective synthesis of 1T′ MoS_2 monolayers and heterophase bilayers. *Nat. Mater.* **17**, 1108-1114 (2018).

12 Lin, Z. *et al.* Solution-processable 2D semiconductors for high performance large-area electronics. *Nature* **562**, 254-258 (2018).

13 Coleman, J. N. *et al.* Two-dimensional nanosheets produced by liquid exfoliation of layered materials. *Science* **331**, 568-571 (2011).

14 Peng, J. *et al.* High phase purity of large-sized 1T′-MoS_2 monolayers with 2D superconductivity. *Adv. Mater.* **31**, e1900568 (2019).

15 Shen, R. *et al.* High-concentration single atomic Pt sites on hollow CuS_x for selective O_2 reduction to H_2O_2 in acid solution. *Chem* **5**, 2099-2110 (2019).

16 Qiao, B. *et al.* Single-atom catalysis of CO oxidation using Pt_1/FeO_x. *Nat. Chem.* **3**, 634-641 (2011).

17 Ren, Y. *et al.* Unraveling the coordination structure-performance relationship in Pt_1/Fe_2O_3 single-atom catalyst. *Nat. Commun.* **10**, 4500 (2019).

18 Borodko, Y., Ercius, P., Pushkarev, V., Thompson, C. & Somorjai, G. From single Pt atoms to Pt nanocrystals: Photoreduction of Pt^{2+} inside of a PAMAM dendrimer. *J. Phys. Chem. Lett.* **3**, 236-241 (2012).

19 Hansen, J. N. *et al.* Is there anything better than Pt for HER? *ACS Energy Lett.* **6**, 1175-1180 (2021).

20 Zheng, J., Yan, Y. & Xu, B. Correcting the hydrogen diffusion limitation in rotating disk electrode measurements of hydrogen evolution reaction kinetics. *J. Electrochem. Soc.* **162**, F1470-F1481 (2015).

21 Zalitis, C. M., Sharman, J., Wright, E. & Kucernak, A. R. Properties of the hydrogen oxidation reaction on Pt/C catalysts at optimised high mass transport conditions and its relevance to the anode reaction in PEFCs and cathode reactions in electrolysers. *Electrochim. Acta* **176**, 763-776 (2015).

22 Tian, Y., Yu, L., Zhuang, C., Zhang, G. & Sun, S. Fast synthesis of Pt single-atom catalyst with high intrinsic activity for hydrogen evolution reaction by plasma sputtering. *Mater. Today Energy* **22**, 100877 (2021).

23 Li, Y. *et al.* Tungsten oxide/reduced graphene oxide aerogel with low-content platinum as high-performance electrocatalyst for hydrogen evolution reaction. *Small* **17**, e2102159 (2021).

24 Lu, F. *et al.* Engineering platinum-oxygen dual catalytic sites via charge transfer towards highly efficient hydrogen evolution. *Angew. Chem. Int. Ed.* **59**, 17865-17871 (2020).

25 Ye, S. *et al.* Highly stable single Pt atomic sites anchored on aniline-stacked graphene for hydrogen evolution reaction. *Energy Environ. Sci.* **12**, 1000-1007 (2019).

26 Cheng, N. *et al.* Platinum single-atom and cluster catalysis of the hydrogen evolution reaction. *Nat. Commun.* **7**, 13638 (2016).

27 Kucernak, A. R. & Zalitis, C. General models for the electrochemical hydrogen oxidation and hydrogen evolution reactions: Theoretical derivation and experimental results under near mass-transport free conditions. *J. Phys. Chem. C* **120**, 10721-10745 (2016).

28 Durst, J., Simon, C., Hasché, F. & Gasteiger, H. A. Hydrogen oxidation and evolution reaction kinetics on carbon supported Pt, Ir, Rh, and Pd electrocatalysts in acidic media. *J. Electrochem. Soc.* **162**, F190-F203 (2015).

29 Nørskov, J. K. *et al.* Trends in the exchange current for hydrogen evolution. *J. Electrochem. Soc.* **152**, J23-J26 (2005).

30 Esparbé, I. *et al.* Structure and electrocatalytic performance of carbon-supported platinum nanoparticles. *J. Power Sources* **190**, 201-209 (2009).

31 Jiang, B., Liao, F., Sun, Y., Cheng, Y. & Shao, M. Pt nanocrystals on nitrogen-doped graphene for the hydrogen evolution reaction using Si nanowires as a sacrificial template. *Nanoscale* **9**, 10138-10144 (2017).

32 Li, S., Lee, J. K., Zhou, S., Pasta, M. & Warner, J. H. Synthesis of surface grown Pt nanoparticles on edge-enriched MoS_2 porous thin films for enhancing electrochemical performance. *Chem. Mater.* **31**, 387-397 (2019).

33 Durst, J. *et al.* New insights into the electrochemical hydrogen oxidation and evolution reaction mechanism. *Energy Environ. Sci.* **7**, 2255-2260 (2014).

34 Neyerlin, K. C., Gu, W., Jorne, J. & Gasteiger, H. A. Study of the exchange current density for the hydrogen oxidation and evolution reactions. *J. Electrochem. Soc.* **154**, B631-B635 (2007).

35 Hinnemann, B. *et al.* Biomimetic hydrogen evolution: MoS_2 nanoparticles as catalyst for hydrogen evolution. *J. Am. Chem. Soc.* **127**, 5308-5309 (2005).

Fig. 1 | Preparation and characterization of exfoliated 1T′-MoS_2 NSs. a, Schematic illustration of preparing 1T′-MoS_2 NSs from K_xMoS_2 crystals through the electrochemical intercalation (Step 1) and subsequent exfoliation (Step 2). **b**, TEM and **c**, atomic force microscope (AFM) images of the exfoliated 1T′-MoS_2 NSs. Insets in (**c**): the height profiles and measured thicknesses of 1T′-MoS_2 NSs. **d**, Thickness distribution histogram of 1T′-MoS_2 NSs measured by AFM (1.4 nm is the mean thickness and 0.4 nm is the standard deviation). **e**, HAADF-STEM image of a typical 1T′-MoS_2 NS. Inset: the corresponding FFT pattern. **f**, XPS spectra of exfoliated 1T′-MoS_2 NSs and 2H-MoS_2 NSs. The empty dots and the solid curves represent the experimental XPS data and the corresponding deconvoluted spectra, respectively. **g**, Raman spectra of exfoliated 1T′-MoS_2 NSs and 2H-MoS_2 NSs.

Fig. 2 | Structural characterizations of s-Pt/1T′-MoS_2. a, TEM image of s-Pt/1T′-MoS_2. Inset: the corresponding SAED pattern. **b**, STEM image and the corresponding EDS elemental mappings of s-Pt/1T′-MoS_2. **c**, Atomic-resolution HAADF-STEM image of s-Pt/1T′-MoS_2 showing the isolated Pt atomically dispersed on 1T′-MoS_2 NS. Three kinds of single-atomically dispersed Pt, denoted as Pt_{sub}, $Pt_{ads\text{-}S}$ and $Pt_{ads\text{-}Mo}$, respectively, are enclosed by the white dotted rectangles. **d**-**f**, Simulated atomic structures (**d_1**-**f_1**), the corresponding simulated STEM images (**d_2**-**f_2**), and the intensity profiles (**d_3**-**f_3**) of Pt_{sub} (**d**), $Pt_{ads\text{-}S}$ (**e**), and $Pt_{ads\text{-}Mo}$ (**f**), respectively. The yellow, blue, and red balls in (**d_1**-**f_1**) represent the S, Mo, and Pt atoms, respectively. The dashed curves of the simulated intensity profiles in (**d_3**-**f_3**) are taken from the corresponding white dotted rectangles in the simulated STEM images (**d_2**-**f_2**). The histograms of the experimental intensity profiles in (**d_3**-**f_3**) are taken from the corresponding white dotted rectangles in (**c**).

Fig. 3 | Electronic structural characterizations of s-Pt/1T′-MoS_2. a, Pt L_3-edge XANES, and **b**, Fourier-transformed EXAFS spectra of s-Pt/1T′-MoS_2, commercial PtS_2 powder, PtNPs/2H-MoS_2, and Pt foil. **c**, Pt 4*f*, and **d**, Mo 3*d* XPS spectra of s-Pt/1T′-MoS_2 and PtNPs/2H-MoS_2. The empty dots and curves in (**c**,**d**) show the experimental XPS data and the corresponding deconvoluted spectra, respectively.

Fig. 4 | Measurements of electrocatalytic HER. a, Schematic illustration of the floating electrode setup. **b**, HER polarization curves for s-Pt/1T′-MoS_2 (**E1**) and HiSPEC 9100 Pt/C (**E2**), showing the $j_{geometric}$. Inset: the cyclic voltammogram of s-Pt/1T′-MoS_2. **c**, HER polarization curves for s-Pt/1T′-MoS_2 (**E1**) and HiSPEC 9100 Pt/C (**E2**), showing the $j_{mass,Pt}$. **d**, Comparison of the mass activities at the overpotential of -50 mV (η=-50 mV) of s-Pt/1T′-MoS_2 and HiSPEC 9100 Pt/C with previously reported Pt-based electrocatalysts. The error bars of s-Pt/1T′-MoS_2 and HiSPEC 9100 Pt/C in (**d**) are the standard deviations obtained from independent HER measurements on three batches of floating electrodes, *i.e.*, **E1**, **E3**, **E5** for s-Pt/1T′-MoS_2 and **E2**, **E4**, **E6** for HiSPEC 9100 Pt/C. **e**, Mass activities and the corresponding fitting result of s-Pt/1T′-MoS_2 plotted on a logarithmic current scale. The fitting is performed simultaneously for the data on three floating electrodes of s-Pt/1T′-MoS_2 (**E1**, **E3**, **E5**). **f**, Mass activities and the corresponding fitting result of HiSPEC 9100 Pt/C plotted on a logarithmic current scale. The fitting is performed simultaneously for the data on three floating electrodes

of HiSPEC 9100 Pt/C (**E2**, **E4**, **E6**). **g**, Comparison of the $j_{0,mass}$ of s-Pt/1T′-MoS_2 and HiSPEC 9100 Pt/C with the previously reported electrocatalysts measured by different techniques. The HER measurements are conducted in 1 M $HClO_4$ at 298 K under H_2 (101 kPa) at a scan rate of 20 mV s^{-1}. Note: The Pt loadings on floating electrodes are 533±118 ng_{Pt} cm^{-2} for s-Pt/1T′-MoS_2, and 563±273 ng_{Pt} cm^{-2} for HiSPEC 9100 Pt/C, respectively. Abbreviations in (**a**): **RE**, reference electrode; **CE**, counter electrode; **WE**, working electrode; **PCTE**, polycarbonate track etch; **Teflon AF**, Teflon AF-2400 (DuPont). Abbreviations in (**d**) and (**g**): **FE**, floating electrode; **RDE**, rotating disk electrode; **GCE**, glassy carbon electrode.

Methods

■ Materials synthesis.

Chemicals. Potassium molybdate (K_2MoO_4, 98%), sulfur powder (S, 99.5%), isopropanol (IPA, 99.8%), acetonitrile (99.8%), potassium tetrachloroplatinate (II) (K_2PtCl_4, 99.99% trace metals basis), poly(vinylidene fluoride) (PVDF), and tetraheptylammonium bromide were purchased from Sigma-Aldrich. Purified argon (Ar, 99.9%) and hydrogen (20% H_2/80% Ar) were purchased from Leeden National Oxygen Ltd. (Singapore). Copper foils were purchased from ACME Research Support Pte Ltd (Singapore). Ethanol (99.9%) and acetone (Tech Grade) were purchased from Merck (Germany). N,N-dimethylformamide (DMF) was purchased from Fisher Scientific. 2H-phase molybdenum disulfide (MoS_2) powder (10-30 μm) was purchased from Rose Mill (USA). All chemicals and materials were used as received without any further purification. The Milli-Q water (resistivity of 18.2 MΩ·cm, Milli-Q System, Millipore, Billerica, MA, USA) was used in our experiment. The sulfuric acid electrolyte (0.5 M H_2SO_4 or 1 M H_2SO_4) was prepared by diluting Merck Suprapur H_2SO_4 (≥95%) in Milli-Q water. The perchloric acid electrolyte (1 M $HClO_4$) was prepared by diluting the Merck Suprapur $HClO_4$ 70% in Milli-Q water. The 34%-27% HCl (VWR CHEMICALS, NORMATOM®, USA) and 65% HNO_3 (MERCK, Suprapur®, USA) were used for digestion. Ultrahigh-purity gases, *i.e.*, hydrogen (BIP PLUS, 6.6 N purity) and nitrogen (BIP PLUS 6.8 N purity), were purchased from Air Products (USA).

Synthesis of K_xMoS_2 crystals. The K_xMoS_2 crystals were synthesized according to our previously reported method with slight modification[10]. After K_2MoO_4 (500 mg) and S powder (500 mg) were mixed and ground, the mixture was placed in a quartz tube and annealed in a tube furnace at 450 °C for 1.5 h under a gas flow of H_2 (10 s.c.c.m.) and Ar (190 s.c.c.m.). After cooling down to room temperature, the product was taken out and then mixed with S powder (500 mg). The obtained mixture was placed in a quartz tube and annealed in the tube furnace at 450 °C for 1.5 h under atmosphere of H_2 (10 s.c.c.m.) and Ar (190 s.c.c.m.). Subsequently, the reaction zone was heated to 850 °C at a heating rate of 30 °C min^{-1} under

atmosphere of H_2 (40 s.c.c.m.) and Ar (160 s.c.c.m.), and then maintained at 850 °C for 10 h. After cooling down to room temperature, the obtained powder was collected and washed with Milli-Q water until the pH value of the suspension reached 7-8. The obtained powder was then stored in Milli-Q water for 24 h. After washing with Milli-Q water again and drying at room temperature under vacuum, the K_xMoS_2 crystals were obtained and collected for the further usage.

Preparation of 1T′-MoS_2 NSs by electrochemical intercalation. The electrochemical intercalation process was conducted in a two-electrode electrochemical cell based on the previous report with modification[12]. After the K_xMoS_2 crystals and PVDF as a binder were mixed in DMF, the mixture was uniformly coated on a copper foil and dried under vacuum, which was then used as the cathode. The mass ratio of K_xMoS_2 crystals, PVDF, and DMF were 8:1:80. The graphite rod was used as anode. The tetraheptylammonium bromide, which was dissolved in acetonitrile with a concentration of 5 mg ml^{-1}, served as electrolyte. The intercalation process was performed at an applied voltage of 8 V for 1 h. The intercalated sample was then transferred into a centrifuge tube followed by sonication in 5 ml of DMF for less than 5 s. The dispersion was centrifuged at 6,000 r.p.m. for 10 min. The obtained precipitate was re-dispersed in 5 ml of Milli-Q water. The final product was collected by centrifugation at 6,000 r.p.m. for 10 min and re-dispersed in Milli-Q water for the further usage.

Preparation of 2H-MoS_2 NSs by electrochemical intercalation. The intercalation and exfoliation to prepare 2H-MoS_2 NSs were similar to the aforementioned processes used for preparation of 1T′-MoS_2 NSs, except that the K_xMoS_2 crystals were replaced by the commercial 2H-MoS_2 powder, and the sonication time was prolonged to 30 min.

Synthesis of different Pt structures on 1T′-MoS_2 NSs. In a typical experiment to prepare s-Pt/1T′-MoS_2, 120 μl aqueous solution of 0.05 M K_2PtCl_4 were injected into 10 ml of 1T′-MoS_2 water-ethanol (v/v = 9:1) solution (0.10 mg ml^{-1}, determined by inductively coupled plasma-optical emission spectrometry (ICP-OES)) in a 15-ml glass vial. The obtained mixture was then irradiated under a 150 W halogen lamp at 10% of its full intensity for 14 h under ambient

conditions. After the photoreduction reaction, the resulting solution was centrifuged at 6,000 r.p.m. for 15 min. The precipitates were washed with IPA and collected for the further usage. Based on the ICP-OES result, the Pt loading in the prepared s-Pt/1T′-MoS_2 was determined to be ~10.0 wt% (Supplementary Table 1).

The aforementioned synthetic method has also been used to prepare different Pt structures on the 1T′-MoS_2 NSs with the Pt loadings of 4.3 wt% (denoted as s-Pt-4/1T′-MoS_2), 6.4 wt% (denoted as s-Pt-6/1T′-MoS_2), 12.2 wt% (denoted as PtNPs-12/1T′-MoS_2), and 15.5 wt% (denoted as PtNPs-15/1T′-MoS_2) (as determined by the ICP-OES, Supplementary Table 1), when 120 μl aqueous solution of 0.05 M K_2PtCl_4 was changed to 80, 100, 200, and 300 μl, respectively.

Synthesis of PtNPs/2H-MoS_2. The synthesis process was similar to that used for synthesis of the s-Pt/1T′-MoS_2, except that the 1T′-MoS_2 NSs were replaced by 2H-MoS_2 NSs. Based on the ICP-OES result, the Pt loading in the prepared PtNPs/2H-MoS_2 was determined to be ~9.6 wt% (Supplementary Table 1).

■ Characterizations.

TEM and HRTEM images, SAED patterns, STEM images and the corresponding EDS data were recorded on JEOL JEM-2100F (JEOL, Tokyo, Japan) at an acceleration voltage of 200 kV. HAADF-STEM images were obtained on a JEOL ARM-200F (JEOL, Tokyo, Japan) operated at 200 kV with cold field emission gun and double hexapole spherical aberration correctors (CEOS GmbH, Heidelberg, Germany). The STEM image simulations were conducted with QSTEM, a STEM image simulation software[36]. SEM images and the corresponding EDS spectra were recorded on JEOL JSM-7600F (JEOL, Tokyo, Japan). Optical microscopy images were taken on a Nikon Eclipse LV100D microscope. AFM (Cypher, Asylum Research, USA) was used to characterize the thickness of 1T′- and 2H-MoS_2 NSs in tapping mode in air. UV-Vis absorption spectra were recorded on a UV-2700 (Shimadzu, Tokyo, Japan) with QS-grade quartz cuvettes (111-QS, Hellma Analytics) at room temperature. XPS measurements were conducted on the ESCALAB 250Xi (Thermo Fisher Scientific, USA)

instrument. Raman spectra were recorded by the WITec system (Germany) with a wavelength of 532 nm and power of < 0.1 mW to avoid the phase transition of MoS_2 during the measurement. The Raman band of a Si wafer at 520 cm^{-1} was used as the reference to calibrate the spectrometer. XANES and EXAFS measurements of the platinum L_3 edge were carried out using the X-ray absorption fine structure for catalysis beamline in Singapore Synchrotron Light Source[37]. Processing and analysis of data were carried out on Athena and Artemis (version 0.9.26)[38]. Simulation of XANES was implemented in the finite difference method near edge structure (FDMNES) code[39], in which the Schrödinger equation was solved by the finite difference method (FDM) within the local density approximation. ICP-OES was performed on a Dual-view Optima 5300 DV ICP-OES system (USA). Inductively coupled plasma mass spectrometry (ICP-MS) was performed on the Agilent 8900 triple quadrupole ICP-MS equipment.

■ Electrochemical measurements.

Measurements with floating electrode.

As shown in Fig. 4, the floating electrode technique uses a small quantity of catalyst deposited uniformly and homogeneously across a small catalyst area, *i.e.*, 1 mm in diameter, *via* the vacuum filtration on a porous gas diffusion electrode. The porous electrode is floating on the aqueous electrolyte which allows gas, *i.e.*, H_2, to flow freely to and from the catalysts, while the catalyst layer is in contact with the aqueous phase electrolyte, *i.e.*, 1 M $HClO_4$ aqueous solution. The detailed preparation and measurement processes of the floating electrode are described below.

Catalyst suspension. The s-Pt/1T′-MoS_2 catalyst was first dispersed in a mixture of Milli-Q water and IPA (v/v = 1:3) and then diluted to 100 μg_{Pt} L^{-1} with Milli-Q water. Commercially available Pt/C catalyst (HiSPEC 9100, Johnson Matthey Fuel Cells) was first dispersed in a mixture of Milli-Q water and IPA (v/v = 1:1) and then diluted to 100 μg_{Pt} L^{-1} with Milli-Q water.

Fabrication of the floating electrode. After sonicating on full power (35 kHz, 100%) at 4 ºC

for 20 min, a 30 μL aliquot of the diluted catalyst suspension is deposited on a gold (50 nm thick) sputter-coated porous polycarbonate substrate (Sterlitech, 0.4 μm pore size, PCTF0447100) by vacuum filtration (~10 min) through a mask of a diameter of 1 mm under a pressure of 1 bar. The geometric area of the catalyst spot was kept at 0.00785 cm^2 (1 mm in diameter). A 0.1 wt% Teflon AF 2400 (DuPont) suspension in Fluorinert FC-40 (Sigma-Aldrich) was evenly applied to the side of the substrate without catalysts to make the electrode hydrophobic. The amount of Teflon AF 2400 on the electrode was 1.1 μg cm^{-2}, optimized for the HER measurements. The electrode was then dried in a laminar flow hood (Thermo Scientific Heraguard Clean bench, HEPA H14, removal of >99.995% 0.3 μm particles) for at least 24 h before usage.

Electrochemical cell. In a three-electrode electrochemical cell, the working electrode (WE) was the as-fabricated floating electrode, the reference electrode (RE) was an in-house made reversible hydrogen electrode (RHE), and the counter electrode (CE) was a coiled gold wire. The components of the floating electrode setup, which might be in contact with the electrolyte, were first soaked in an ALNOCHROMIX acid bath overnight. Then, they were rinsed vigorously with Milli-Q water and boiled 6 times in Milli-Q water before usage. 1 M $HClO_4$ was used as electrolyte. The temperature of the cell was controlled at 25 ºC by connecting the water jacket of the cell to a water recirculator (huber CC-K6 with Pilot ONE) during the measurements.

Electrochemical measurements of the floating electrode. The electrochemical measurements were conducted with a Metrohm Autolab potentiostat. The electrolyte was first degassed by purging nitrogen gas for at least 30 min, and the headspace of the cell was purged with hydrogen for at least 1 min before the floating electrode was put into the cell and contacted the electrolyte to ensure the initial open circuit voltage at around 0 V (*vs*. RHE). To activate the catalysts, 100 scans of cyclic voltammetry were conducted from -0.25 V to 0.1 V (*vs.* RHE) at 50 mV s^{-1} under pure hydrogen. The reported measurements were then collected at 20 mV s^{-1} under pure hydrogen. For the HiSPEC 9100 Pt/C catalyst, a further activation process stated in our recent work[40] was conducted.

Catalyst loading measurements. The loading of the catalyst was determined by post-electrochemical measurements. The catalyst spot, *i.e.*, the tip of the floating electrode, was cut off the electrode and digested (with sonication for 5 min) in a fresh mixture of a 120 µL of 34%-27% HCl (VWR CHEMICALS, NORMATOM®) and a 40 µL of 65% HNO_3 (MERCK, Suprapur®). The mixture was allowed to sit overnight to ensure complete dissolution of the catalyst and decomposition of the aqua regia. The solution was further diluted into a sample of 5 mL and sent to ICP-MS to obtain a concentration of Pt in ppb. The Pt loadings of the floating electrodes were then calculated from the concentrations.

Fitting of the hydrogen oxidation reaction (HOR)/HER data. Fitting of the HOR/HER response was conducted by using a model developed in our previous work[27] with a fixed symmetry factor of 0.5. This model solves the individual Tafel and Volmer steps under the steady state approximation that the hydrogen coverage is time invariant and provides direct information about the energy of hydrogen adsorption and the exchange current density of the reaction.

Durability test. The durability tests were performed in a typical three-electrode system. The s-Pt/1T′-MoS_2 IPA dispersion was drop-casted on the glassy carbon electrode or carbon paper electrode and used as working electrode. The graphite rod and Ag/AgCl (3 M KCl) were used as counter electrode and as reference electrode, respectively. The durability tests were conducted by applying the cyclic potential sweeps between 0.1 V and -0.1 V (*vs.* RHE) at a scan rate of 100 mV s^{-1} for 10,000 cyclic voltammetry cycles in a N_2-saturated 0.5 M H_2SO_4 aqueous solution. The polarization curves of s-Pt/1T′-MoS_2 were recorded before and after the durability test at a scan rate of 5 mV s^{-1}. After the durability test, the s-Pt/1T′-MoS_2 catalyst was scratched from the electrode surface and washed with IPA for three times. The collected s-Pt/1T′-MoS_2 was then used for further measurements.

Electrochemical measurements in H-type electrochemical cell.

The HER activity and stability of s-Pt/1T′-MoS_2 and commercial HiSPEC 9100 Pt/C at high current densities were tested in an H-type cell separated by an ion exchange membrane (Nafion

117, DuPont). The working electrode was prepared by drop-casting the s-Pt/1T′-MoS_2 or HiSPEC 9100 Pt/C dispersion on the Toray TGP-H-060 carbon paper (FuelCellStore), in which the Pt loading was kept at 0.0175 mg cm^{-2} measured by ICP-OES. After the catalyst-modified carbon fiber paper was dried at room temperature, 5.7 μl of Nafion ethanolic solution (0.1 wt%) were dropped on its surface to protect the catalyst. Pt mesh and Ag/AgCl (3 M KCl) were used as the counter electrode and reference electrode, respectively. The Ag/AgCl (3 M KCl) electrode was calibrated with respect to the RHE. The linear sweep voltammetric (LSV) curves were measured in a N_2-saturated 0.5 M H_2SO_4 aqueous solution at a scan rate of 5 mV s^{-1}, and then iR-corrected on the basis of the electrochemical impedance spectroscopy (EIS) data. The chronopotentiometric test at 1,500 mA cm^{-2} was conducted in a N_2-saturated 0.5 M H_2SO_4 aqueous solution for 240 h. After the long-term stability test, the LSV curve of s-Pt/1T′-MoS_2 was measured again.

Electrochemical measurements in PEM electrolyser.

First, the Nafion 117 membranes (DuPont) were sequentially treated with 3 wt% H_2O_2, 0.5 M H_2SO_4, and Milli-Q water at 80 °C for 1 h. After cooling to room temperature, the treated N117 membranes were washed and preserved in Milli-Q water. The s-Pt/1T′-MoS_2 and commercial HiSPEC 9100 Pt/C catalysts were used as the cathode materials for the PEM electrolyser.

To prepare the s-Pt/1T′-MoS_2 catalyst ink, 1 mg of s-Pt/1T′-MoS_2 was dispersed in 400 μl of IPA. After adding 4 μl of 5 wt% Nafion solution, the dispersion was ultrasonicated in ice water for 30 s, forming a well-dispersed s-Pt/1T′-MoS_2 catalyst ink. To prepare the HiSPEC 9100 Pt/C catalyst ink, 1 mg of HiSPEC 9100 Pt/C was dispersed in 400 μl of IPA. After adding 4 μl of 5 wt% Nafion solution, the dispersion was ultrasonicated in ice water for 30 min, forming a well-dispersed HiSPEC 9100 Pt/C catalyst ink. The prepared catalyst ink was then dropped on the carbon cloth (FuelCellStore, USA) and dried in the vacuum overnight. The Pt loadings for s-Pt/1T′-MoS_2 and HiSPEC 9100 Pt/C were kept at 0.04 mg cm^{-2} measured by ICP-OES. The catalyst-coated carbon cloth (1 cm^2) was used as the cathode. The commercial IrO_2/carbon paper electrode (1 cm^2, Dioxide Materials, USA) was used as the anode.

After the membrane electrode assembly was constructed with the s-Pt/1T′-MoS_2 or HiSPEC 9100 Pt/C-coated carbon cloth (cathode), treated Nafion 117 membrane (separator), and commercial IrO_2/carbon paper electrode (anode), it was applied in the PEM electrolyser. The PEM electrolyser was operated at room temperature using 1 M H_2SO_4 as the electrolyte solution under the flowing rate of 8 ml min^{-1}. LSV curves were measured at a scan rate of 5 mV s^{-1}. The stability of the PEM electrolyser using s-Pt/1T′-MoS_2 as the anode catalyst was evaluated by measuring chronopotentiometry at 100 mA cm^{-2} for 500 h.

■ DFT calculations.

DFT calculations were performed by using the projector augmented wave (PAW) method[41] as implemented in the Vienna ab initio simulation package (VASP 5.4)[42]. The generalized gradient approximation in the revised-Perdew-Burke-Ernzerhof (RPBE)[43] form was used, and a cutoff energy of 400 eV for plane-wave basis set was adopted. The convergence thresholds were 10^{-5} eV and 0.01 eV/Å for energy and force, respectively. A vacuum space of at least 15 Å was used, so that the interaction between two periodic units can be neglected. Supercells consisting of 2×3×1 of the 1T′-MoS_2 monolayer were used to simulate the 1T′-MoS_2 NS, and the Brillouin zones were sampled by a 5×5×1 Monkhorst-Pack k-point grid.

The ΔG_H was adopted to theoretically evaluate the catalytic performance for HER, which was calculated using the following equation,

$$\Delta G_H = \Delta E + \Delta E_{ZPE} - T\Delta S$$

where the ΔE is the adsorption energy of hydrogen, ΔE_{ZPE} is the correction of zero-point energy, ΔS represents the difference in entropies between the adsorbed state and the corresponding free-standing state, and T is the absolute temperature (300 K).

References

36 Koch, C. T. *Determination of core structure periodicity and point defect density along dislocations*, Arizona State University, (2002).

37 Du, Y. *et al.* XAFCA: a new XAFS beamline for catalysis research. *J. Synchrotron Radiat.* **22**, 839-843 (2015).

38 Ravel, B. & Newville, M. ATHENA, ARTEMIS, HEPHAESTUS: data analysis for X-ray absorption spectroscopy using IFEFFIT. *J. Synchrotron Radiat.* **12**, 537-541 (2005).

39 Bunau, O. & Joly, Y. Self-consistent aspects of X-ray absorption calculations. *J. Phys.: Condens. Matter* **21**, 345501 (2009).

40 Lin, X., Zalitis, C. M., Sharman, J. & Kucernak, A. Electrocatalyst performance at the gas/electrolyte interface under high-mass-transport conditions: Optimization of the "floating electrode" method. *ACS Appl. Mater. Interfaces* **12**, 47467-47481 (2020).

41 Blöchl, P. E. Projector augmented-wave method. *Phys. Rev. B* **50**, 17953-17979 (1994).

42 Kresse, G. & Furthmuller, J. Efficient iterative schemes for ab initio total-energy calculations using a plane-wave basis set. *Phys. Rev. B* **54**, 11169-11186 (1996).

43 Hammer, B., Hansen, L. B. & Nørskov, J. K. Improved adsorption energetics within density-functional theory using revised Perdew-Burke-Ernzerhof functionals. *Phys. Rev. B* **59**, 7413-7421 (1999).

Data availability All data that support the findings of this study are available from the corresponding author upon reasonable request. Source data are provided with this paper.

Acknowledgments H.Z. thanks the support from the Project 52131301 supported by NSFC, the Science Technology and Innovation Committee of Shenzhen Municipality (grant no. SGDX2020110309300301, "Preparation of single atoms on transition metal chalcogenides for electrolytic hydrogen evolution", CityU), the Research Grants Council of Hong Kong (AoE/P-701/20, GRF Project No. 11315722), ITC via the Hong Kong Branch of National Precious Metals Material Engineering Research Center (NPMM), the Start-Up Grant (Project No. 9380100), and the grants (Project Nos. 9678272, 9680314, 7020054 and 1886921) from the City University of Hong Kong. X. Z acknowledge the support from the Start-up Fund (BDC2) and Research Institute for Advanced Manufacturing (RIAM) Fund (CD4D) from the Hong Kong Polytechnic University.

Author contributions H.Z. proposed the research direction and supervised the project. Z.S. and X.Z. designed and performed the experiments. Z.S., X.L. and G.L. carried out the electrochemical experiments. A.R.J.K. developed the model to fit the electrochemical data. C.L. performed the DFT calculation. S.X. performed XAS characterization and data analysis. B.C. performed the STEM characterization. G.N. and Z.S. carried out the Raman measurement. J.L., Z.G., and C.-S.L. conducted the XPS measurement. Z.S., X.Z., and H.Z. analyzed and discussed all experimental results and drafted the manuscript. X. R., L.Z., L.L., Z.L., and X.W. performed some supporting experiments. X.L., Y.G., C.T., G.L., Z.L., Z.H., Q.H., and A.R.J.K. helped to draft the manuscript. All authors checked the manuscript and agreed with its content. The authors declare no competing financial interests.

Competing interests The authors declare no competing interests.

Additional information

Supplementary information Supplementary Information is available for this paper.

Correspondence and requests for materials should be addressed to Hua Zhang and Anthony R. J. Kucernak.

Peer review information *Nature* thanks the anonymous reviewers for their contribution to the peer review of this work.

Extended Data Fig. 1 | Characterization of the obtained 2H-MoS_2 NSs. a, SEM image of the exfoliated 2H-MoS_2 NSs. **b**, TEM and **c**, HRTEM images of a representative 2H-MoS_2 NS. Inset in (**b**) shows the corresponding SAED pattern. The measured lattice spacing of 2.71 Å in (**c**) can be assigned to the {100} planes of the 2H-MoS_2 NSs, which is consistent with the theoretical structure of 2H-MoS_2 as shown in Supplementary Fig. 4b. **d**, EDS spectrum and the corresponding element percentages (inset in (**d**)) of the 2H-MoS_2 NSs showing an expected Mo/S ratio Of ~1:2. **e**, AFM image and the measured thicknesses (insets in (**c**)) of 2H-MoS_2 NSs. **f**, Thickness distribution histogram of 2H-MoS_2 NSs measured by AFM (1.9 nm is the mean thickness and 0.4 nm is the standard deviation).

Extended Data Fig. 2 | Characterizations of PtNPs/2H-MoS_2. a, TEM image of PtNPs/2H-MoS_2. Inset: the diameter distribution histogram of PtNPs grown on 2H-MoS_2 NSs (1.1 nm is the mean size and 0.4 nm is the standard deviation). **b**, SAED pattern of PtNPs/2H-MoS_2 showing two sets of diffraction spots, which can be assigned to the {111} planes of face-centered cubic (*fcc*) Pt and the {100} planes of 2H-MoS_2. The diffraction spots of Pt align well with those of 2H-MoS_2. **c**, HAADF-STEM image of PtNPs/2H-MoS_2. **d**, The corresponding line scan intensity profiles obtained from the area **i** and **ii** in (**c**), respectively. The (111) facets of PtNPs can be observed in (**c**) with an average lattice spacing of 2.28 Å as shown in (**d**), which are well aligned with the (100) planes of 2H-MoS_2 with a measured lattice spacing of 2.77 Å. These results demonstrated that the ultra-small PtNPs are epitaxially grown on the 2H-MoS_2 NSs.

Extended Data Fig. 3 | Characterizations of s-Pt/1T′-MoS_2 with Pt loading of 4.3 wt%, denoted as s-Pt-4/1T′-MoS_2. a-d, HAADF-STEM image (**a**), EDS mapping (**b**), Raman spectrum (**c**), and Mo 3*d* XPS spectrum (**d**) of the s-Pt-4/1T′-MoS_2**.** Inset in (**a**): the corresponding FFT pattern of s-Pt-4/1T′-MoS_2.

Extended Data Fig. 4 | Characterizations of s-Pt/1T′-MoS_2 with Pt loading of 6.4 wt%, denoted as s-Pt-6/1T′-MoS_2. a-d, HAADF-STEM image (**a**), EDS mapping (**b**), Raman

spectrum (**c**), and Mo 3*d* XPS spectrum (**d**) of the s-Pt-6/1T′-MoS_2. Inset in (**a**): the corresponding FFT pattern of s-Pt-6/1T′-MoS_2.

Extended Data Fig. 5 | Characterizations of PtNPs/1T′-MoS_2 with the Pt loading of 12.2 wt%, denoted as PtNPs-12/1T′-MoS_2. a-d, HAADF-STEM image (**a**), EDS mapping (**b**), Raman spectrum (**c**), and Mo 3*d* XPS spectrum (**d**) of the PtNPs-12/1T′-MoS_2. Inset in (**a**): the corresponding FFT pattern of PtNPs-12/1T′-MoS_2.

Extended Data Fig. 6 | Characterizations of PtNPs/1T′-MoS_2 with the Pt loading of 15.5 wt%, denoted as PtNPs-15/1T′-MoS_2. a-d, HAADF-STEM image (**a**), EDS mapping (**b**), Raman spectrum (**c**), and Mo 3*d* XPS spectrum (**d**) of the PtNPs-15/1T′-MoS_2. Inset in (**a**): the corresponding FFT pattern of PtNPs-15/1T′-MoS_2.

Extended Data Fig. 7 | XPS characterizations of Pt with different loading amounts grown on 1T′-MoS_2 NSs. The Pt 4*f* XPS spectra of s-Pt-4/1T′-MoS_2, s-Pt-6/1T′-MoS_2, s-Pt/1T′-MoS_2, PtNPs-12/1T′-MoS_2, and PtNPs-15/1T′-MoS_2.

Extended Data Fig. 8 | Structural characterizations of s-Pt/1T′-MoS_2 before and after the durability test by XAFS. a, Pt L_3-edge XANES, **b**, Fourier-transformed EXAFS spectra in k space, and **c**, Fourier-transformed EXAFS spectra in R space of the s-Pt/1T′-MoS_2 before and after the durability test. The XANES and EXAFS data exhibit no obvious difference after the durability test indicating that the Pt in the s-Pt/1T′-MoS_2 maintains the single-atomically dispersed nature.

Extended Data Fig. 9 | HAADF-STEM characterizations s-Pt/1T′-MoS_2 after the durability test. a, Atomic-resolution HAADF-STEM image of s-Pt/1T′-MoS_2 after the durability test. Inset: the corresponding FFT pattern. **b-d**, Simulated atomic structures (**b_1-d_1**), the corresponding simulated STEM images (**b_2-d_2**), and the intensity profiles (**b_3-d_3**) of Pt_{sub} (**b**), $Pt_{ads\text{-}S}$ (**c**), and $Pt_{ads\text{-}Mo}$ (**d**), respectively. The yellow, blue, and red balls in (**b_1-d_1**) represent the S, Mo, and Pt atoms, respectively. The dashed curves of the simulated intensity profiles in

(**b_3-d_3**) are taken from the corresponding white dotted rectangles in the simulated STEM images (**b_2-d_2**). The histograms of the experimental intensity profiles in (**d_3-f_3**) are taken from the corresponding white dotted rectangles in (**a**). After the durability test, three kinds of s-Pt, *i.e.*, Pt_{sub}, $Pt_{ads\text{-}S}$, and $Pt_{ads\text{-}Mo}$, can still be identified on 1T′-MoS_2. The experimental intensity profiles (histograms in **b_3-d_3**) show good agreement as compared with the simulation results (dashed curves in **b_3-d_3**). Several other representative $Pt_{ads\text{-}S}$ and $Pt_{ads\text{-}Mo}$ atoms are also marked by the white dotted circles in (**a**). In addition, the 1T′-MoS_2 templates showed no phase change after the durability test as confirmed by the HAADT-STEM (**a**) and the corresponding FFT pattern (inset in (**a**)).

Extended Data Fig. 10 | DFT calculation results of s-Pt/1T′-MoS_2 for HER. (**a**-**c**) DFT models of isolated $Pt_{ads\text{-}S}$ (**a**), isolated $Pt_{ads\text{-}Mo}$ (**b**), and Pt_{sub}+$Pt_{ads\text{-}S}$+$Pt_{ads\text{-}Mo}$ (**c**) used for the ΔG_H and the projected density of states (PDOS) calculation. $Pt'_{ads\text{-}S}$, and $Pt'_{ads\text{-}Mo}$ in (**c**) refer to the $Pt_{ads\text{-}S}$ and $Pt_{ads\text{-}Mo}$ in the model of Pt_{sub}+$Pt_{ads\text{-}S}$+$Pt_{ads\text{-}Mo}$, respectively. The model Pt_{sub}+$Pt_{ads\text{-}S}$+$Pt_{ads\text{-}Mo}$ is established based on the experimental and simulation results shown in Supplementary Fig. 13. The yellow, blue, and red balls in (**a**-**c**) represent the S, Mo, and Pt atoms, respectively. **d**, Calculated ΔG_H diagrams for HER. **e**, PDOS of the *d*-band of Pt atoms with the corresponding configurations as shown in (**a**-**c**). The ε_d values are shown in (**e**). The black dotted line in (**e**) indicates the Fermi level. The ε_d values of isolated $Pt_{ads\text{-}S}$ (-2.62 eV) and isolated $Pt_{ads\text{-}Mo}$ (-2.58 eV) on 1T′-MoS_2 are much lower than that of Pt(111) (-1.86 eV). In addition, the ε_d values of $Pt'_{ads\text{-}S}$ and $Pt'_{ads\text{-}Mo}$ further shift to -2.78 eV and -2.75 eV, respectively, which are lower than that of isolated $Pt_{ads\text{-}S}$ and $Pt_{ads\text{-}Mo}$, respectively. These results reveal that the hydrogen adsorptions of $Pt'_{ads\text{-}S}$ and $Pt'_{ads\text{-}Mo}$ are further weakened, resulting in the more positive ΔG_H shown in (**d**).

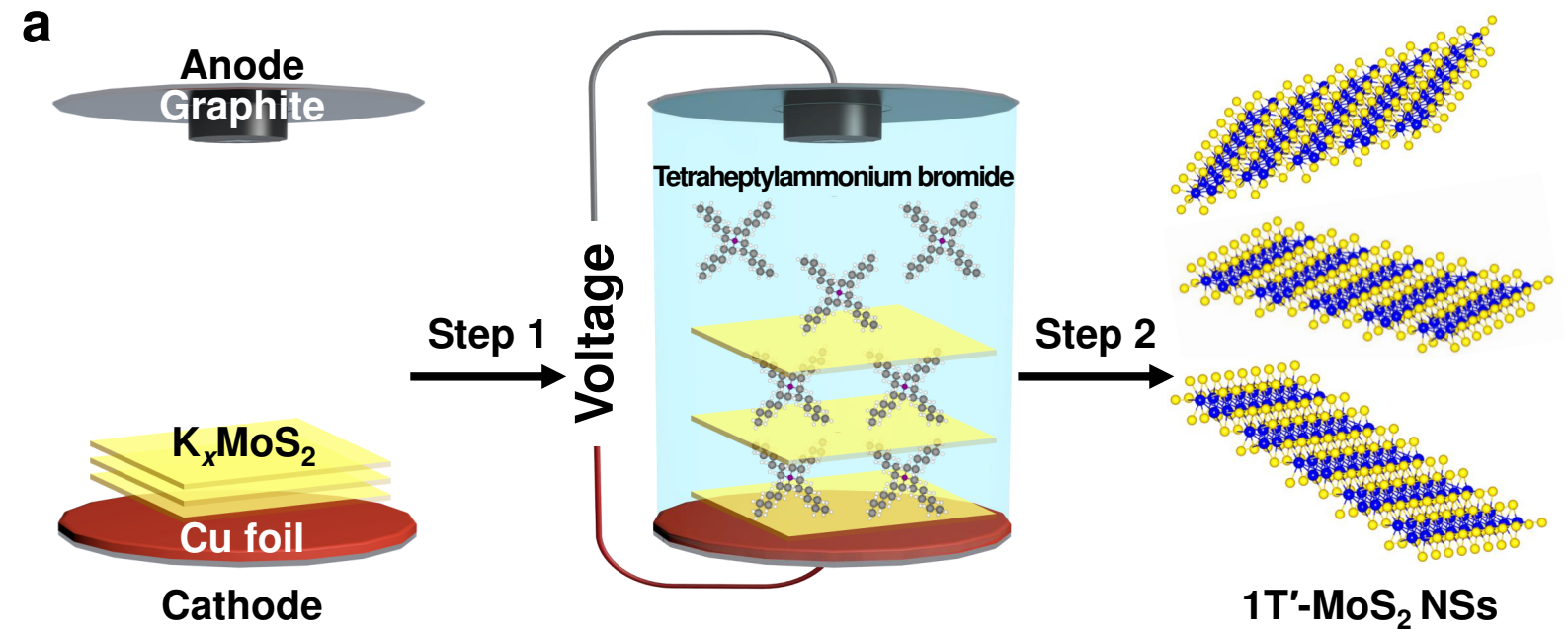
a
Anode
Graphite
Tetraheptylammonium bromide
Step 1
Voltage
Step 2
K_xMoS_2
Cu foil
Cathode
1T′-MoS_2 NSs

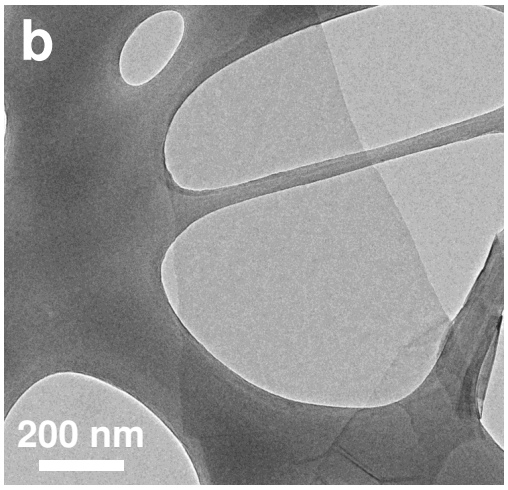
b
200 nm

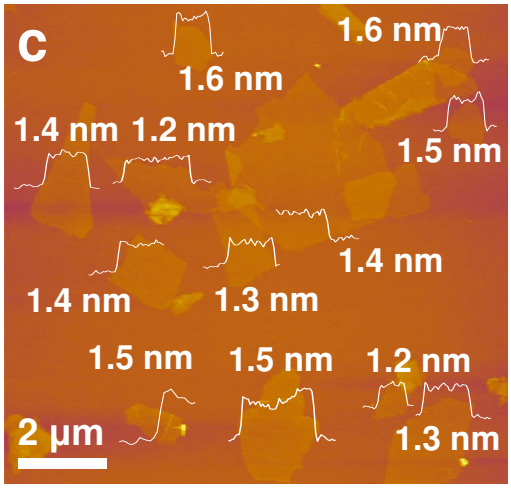
c
1.6 nm
1.6 nm
1.4 nm
1.2 nm
1.5 nm
1.4 nm
1.4 nm
1.3 nm
1.5 nm
1.5 nm
1.2 nm
1.3 nm
2 μm

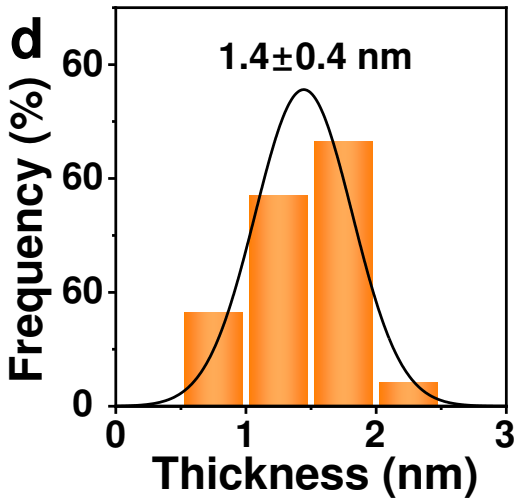
d
1.4±0.4 nm
Frequency (%)
60
60
60
0
0
1
2
3
Thickness (nm)

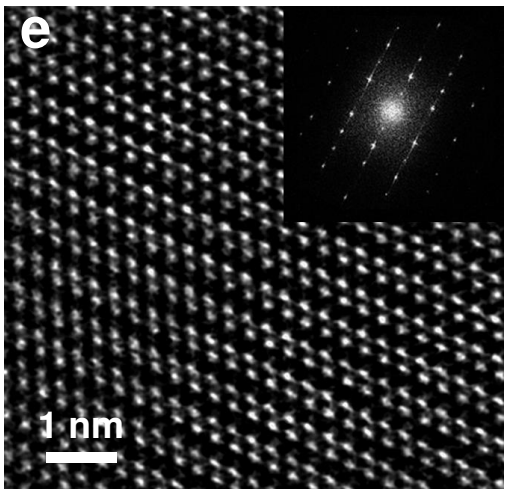
e
1 nm

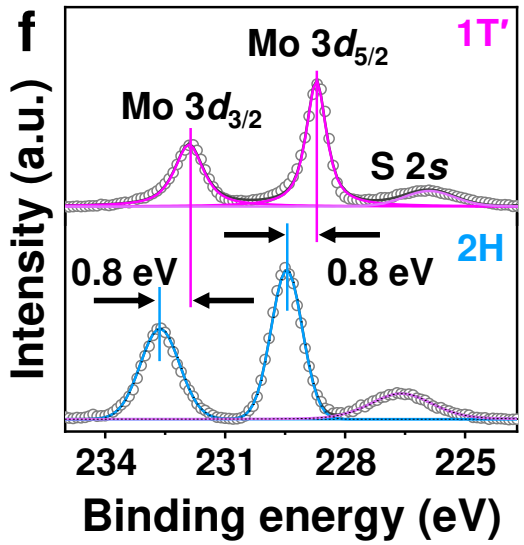
f
Mo 3$d_{5/2}$
1T′
Mo 3$d_{3/2}$
S 2s
2H
0.8 eV
0.8 eV
Intensity (a.u.)
234
231
228
225
Binding energy (eV)

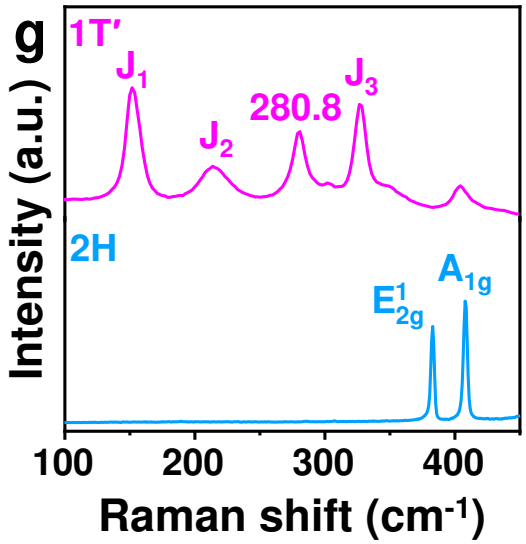
g
1T′
J_1
J_2
280.8
J_3
2H
E^1_{2g}
A_{1g}
Intensity (a.u.)
100
200
300
400
Raman shift (cm^{-1})

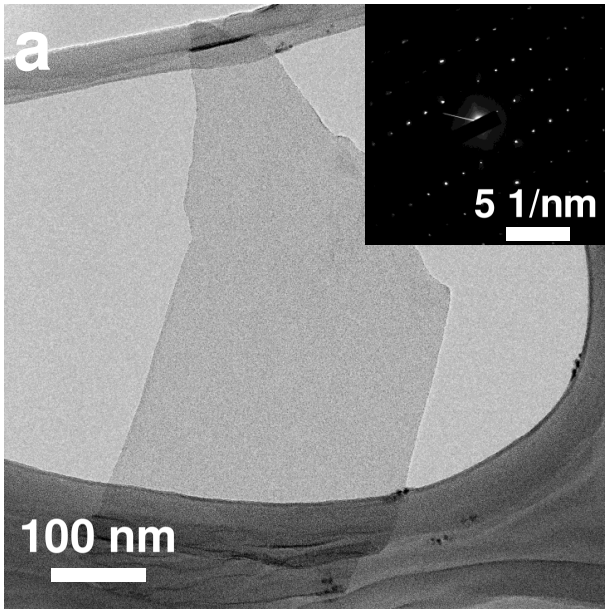
a
5 1/nm
100 nm

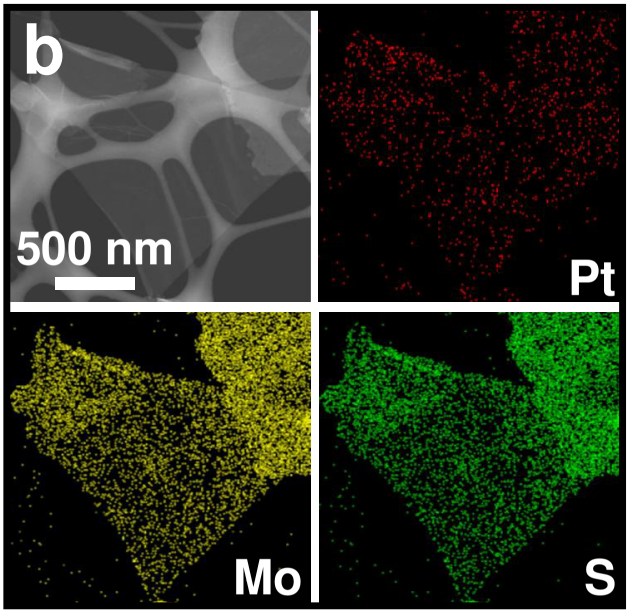
b
500 nm
Pt
Mo
S

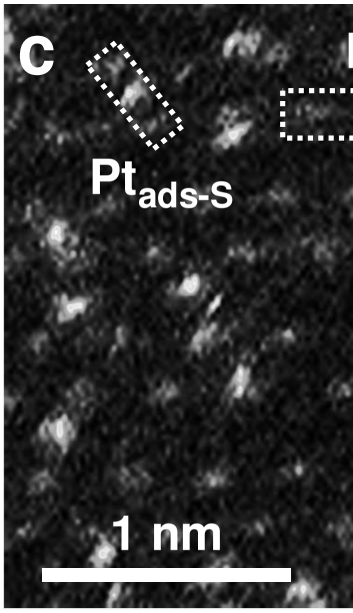
c
Pt$_{ads-S}$
1 nm

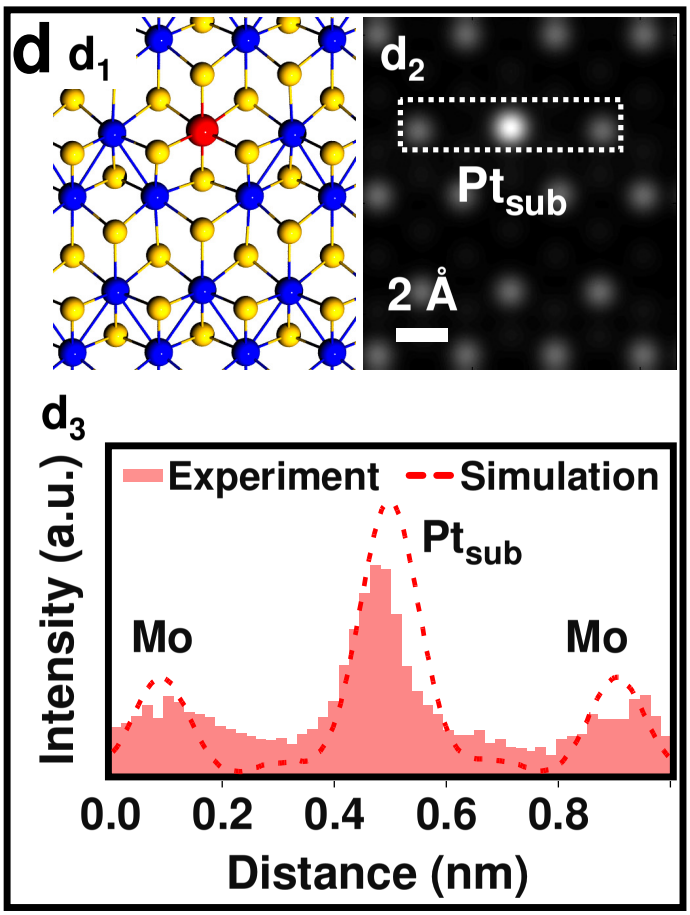
d
d$_1$
d$_2$
Pt$_{sub}$
2 Å
d$_3$
Experiment
Simulation
Pt$_{sub}$
Mo
Mo
Intensity (a.u.)
0.0
0.2
0.4
0.6
0.8
Distance (nm)

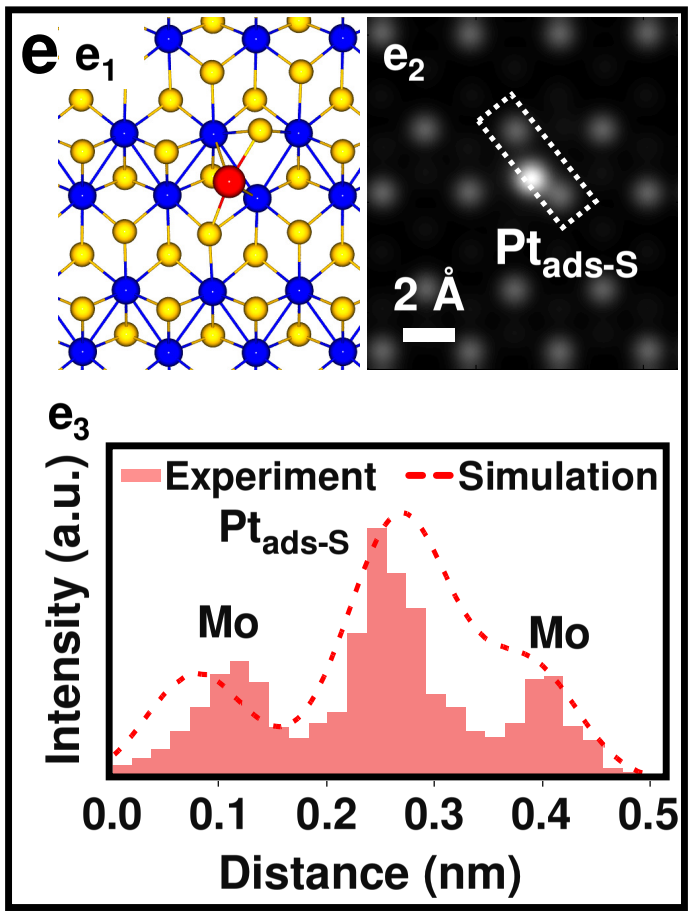
e
e$_1$
e$_2$
Pt$_{ads-S}$
2 Å
e$_3$
Experiment
Simulation
Pt$_{ads-S}$
Mo
Mo
Intensity (a.u.)
0.0
0.1
0.2
0.3
0.4
0.5
Distance (nm)

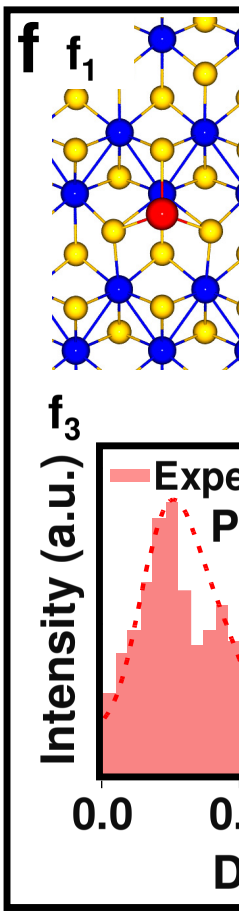
f
f$_1$
f$_3$
Intensity (a.u.)
0.0

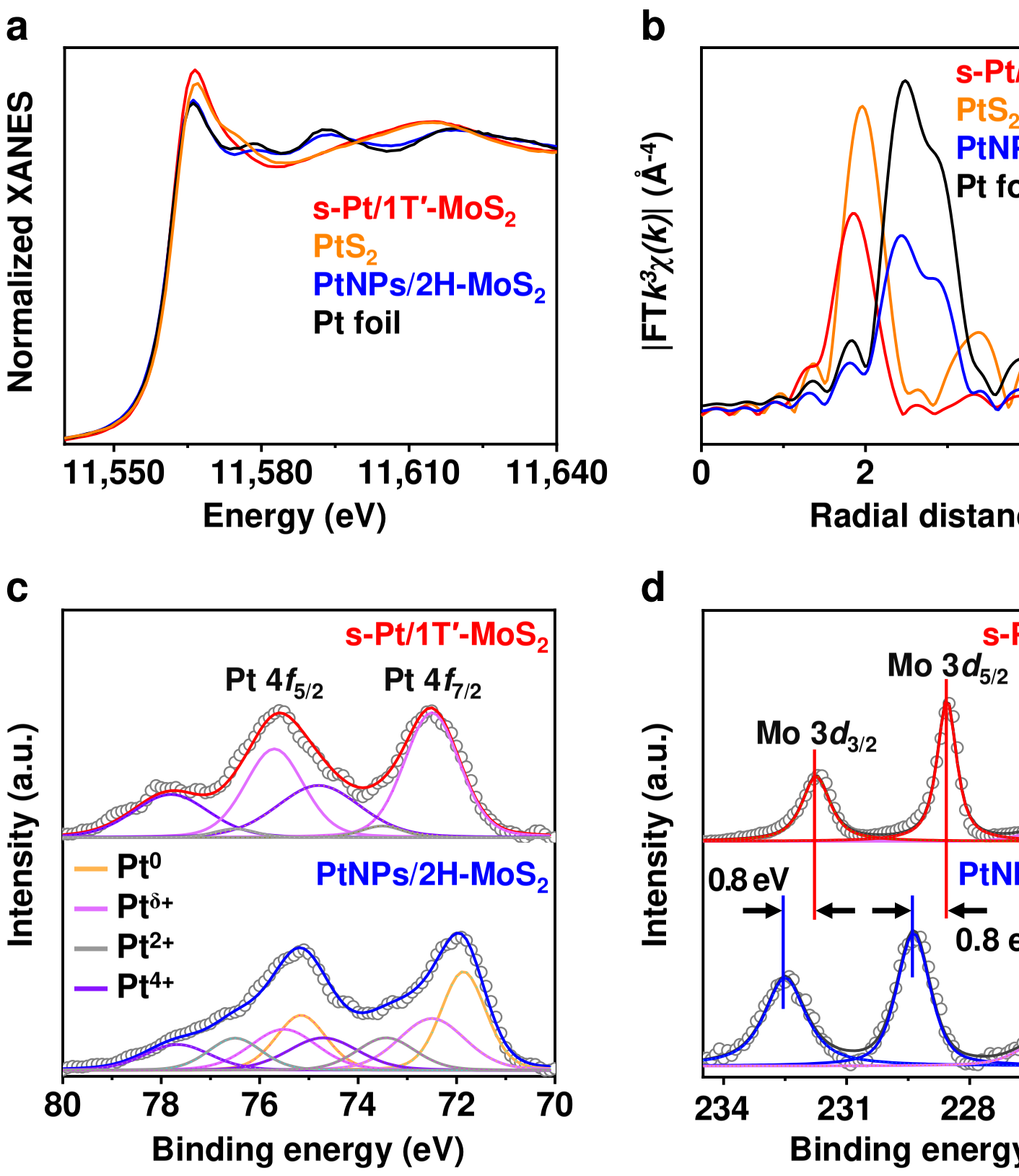
a
Normalized XANES
s-Pt/1T′-MoS2
PtS2
PtNPs/2H-MoS2
Pt foil
11,550
11,580
11,610
11,640
Energy (eV)
b
|FT k3χ(k)| (Å-4)
0
2
Radial distan
c
Intensity (a.u.)
s-Pt/1T′-MoS2
Pt 4f5/2
Pt 4f7/2
PtNPs/2H-MoS2
Pt0
Ptδ+
Pt2+
Pt4+
80
78
76
74
72
70
Binding energy (eV)
d
Intensity (a.u.)
Mo 3d5/2
Mo 3d3/2
0.8 eV
234
231
228
Binding energy

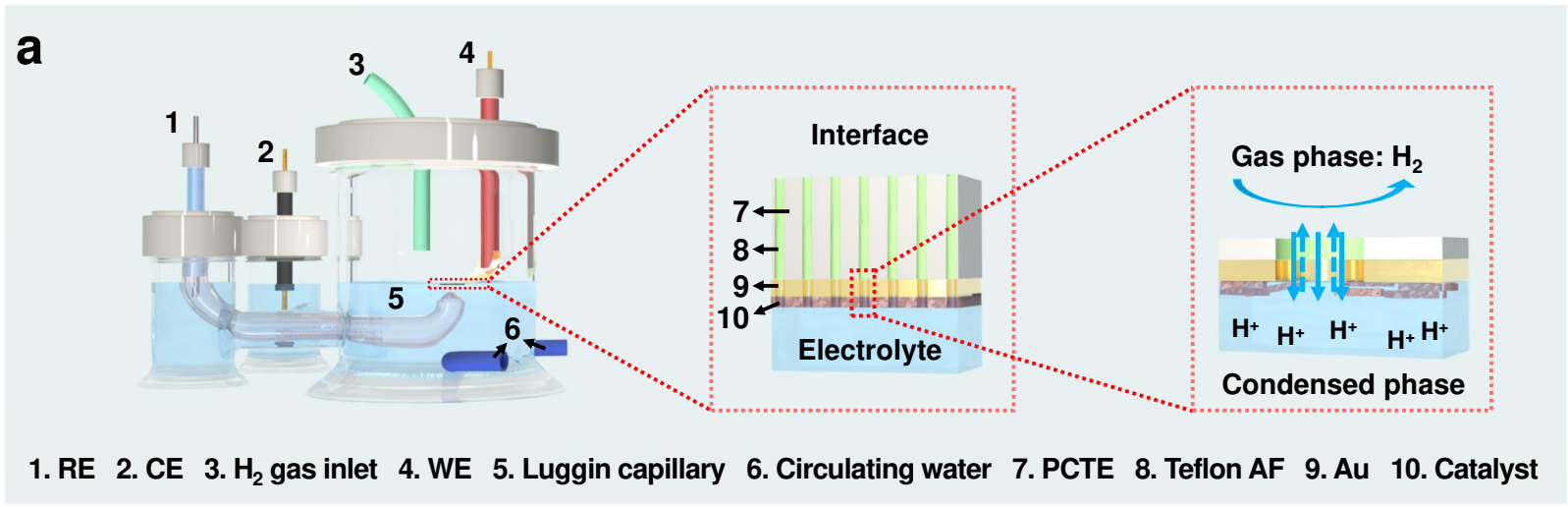
a
1
2
3
4
5
6
Interface
7
8
9
10
Electrolyte
Gas phase: H2
H+ H+ H+ H+ H+
Condensed phase
1. RE 2. CE 3. H2 gas inlet 4. WE 5. Luggin capillary 6. Circulating water 7. PCTE 8. Teflon AF 9. Au 10. Catalyst

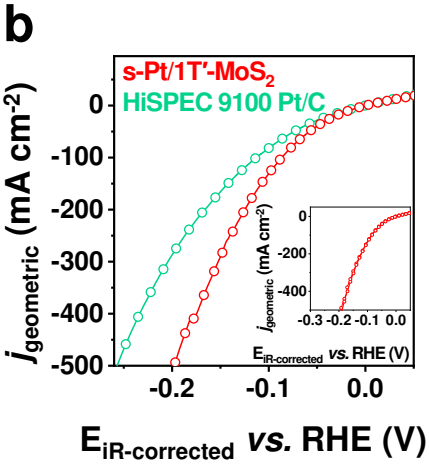
b
s-Pt/1T′-MoS2
HiSPEC 9100 Pt/C
jgeometric (mA cm-2)
0
-100
-200
-300
-400
-500
-0.2
-0.1
0.0
EiR-corrected vs. RHE (V)

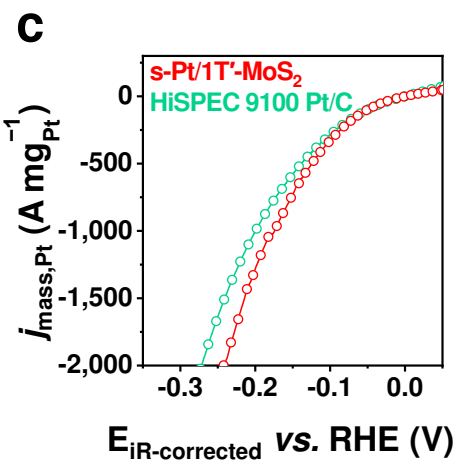
c
s-Pt/1T′-MoS2
HiSPEC 9100 Pt/C
jmass,Pt (A mgPt-1)
0
-500
-1,000
-1,500
-2,000
-0.3
-0.2
-0.1
0.0
EiR-corrected vs. RHE (V)

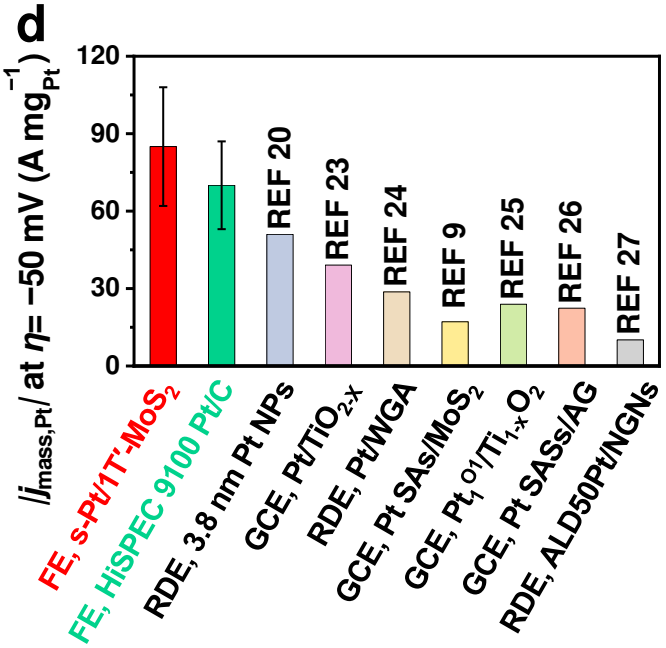
d
|jmass,Pt| at η = −50 mV (A mgPt-1)
120
90
60
30
0
REF 20
REF 23
REF 24
REF 9
REF 25
REF 26
REF 27
FE, s-Pt/1T′-MoS2
FE, HiSPEC 9100 Pt/C
RDE, 3.8 nm Pt NPs
GCE, Pt/TiO2-x
RDE, Pt/WGA
GCE, Pt SAs/MoS2
GCE, Pt1 O1/Ti1-x O2
GCE, Pt SASs/AG
RDE, ALD50Pt/NGNs

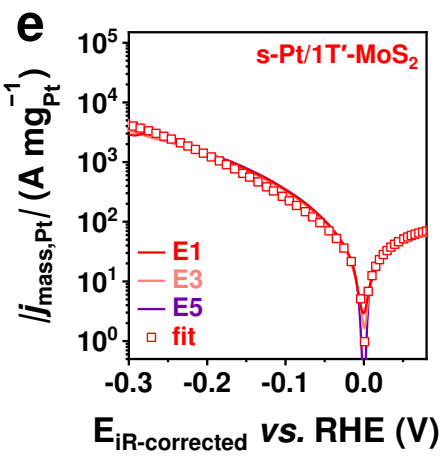
e
s-Pt/1T′-MoS2
|jmass,Pt| (A mgPt-1)
10^5
10^4
10^3
10^2
10^1
10^0
E1
E3
E5
fit
-0.3
-0.2
-0.1
0.0
EiR-corrected vs. RHE (V)

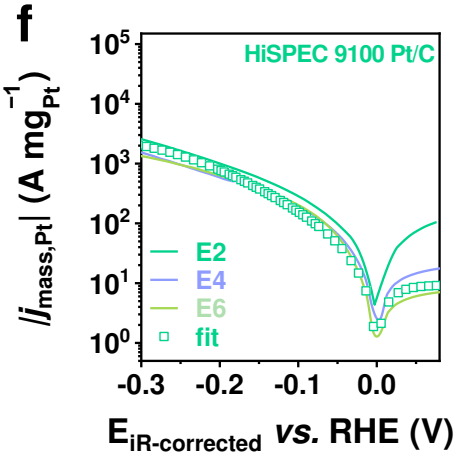
f
HiSPEC 9100 Pt/C
|jmass,Pt| (A mgPt-1)
10^5
10^4
10^3
10^2
10^1
10^0
E2
E4
E6
fit
-0.3
-0.2
-0.1
0.0
EiR-corrected vs. RHE (V)

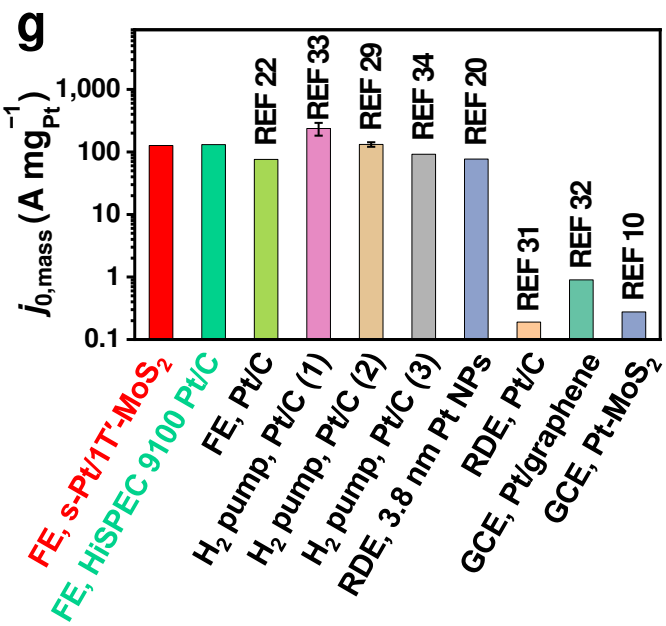
g
j0,mass (A mgPt-1)
1,000
100
10
1
0.1
REF 22
REF 33
REF 29
REF 34
REF 20
REF 31
REF 32
REF 10
FE, s-Pt/1T′-MoS2
FE, HiSPEC 9100 Pt/C
FE, Pt/C
H2 pump, Pt/C (1)
H2 pump, Pt/C (2)
H2 pump, Pt/C (3)
RDE, 3.8 nm Pt NPs
RDE, Pt/C
GCE, Pt/graphene
GCE, Pt-MoS2